Chemical Science

ROYAL SOCIETY OF CHEMISTRY

EDGE ARTICLE

View Article Online
View Journal | View Issue

Cite this: *Chem. Sci.*, 2025, **16**, 13477

All publication charges for this article have been paid for by the Royal Society of Chemistry

Received 2nd April 2025
Accepted 18th June 2025

DOI: 10.1039/d5sc02476e

rsc.li/chemical-science

A nuclear targeted type-I photosensitizer for anti-tumor therapy†

Zipeng Li,‡[a] Wenkai Liu,‡[a] Wanying Ma,[c] Changyu Zhang,[ac] Jiangli Fan *[abc] and Xiaojun Peng [a]

Photodynamic therapy (PDT) has attracted considerable interest in recent years as an effective and promising approach for tumor treatment. In particular, nuclear-targeted type I photosensitizers (PSs) can directly damage the nuclear DNA of tumor cells, thereby significantly enhancing the therapeutic efficacy of PDT. However, nuclear DNA-targeted PSs are rarely reported owing to the lack of clear design principles. Here, we developed a novel DNA-targeted photosensitizer (**Se-PC**) for highly efficient tumor PDT. After incubation with CT DNA, the fluorescence of **Se-PC** was dramatically enhanced, indicating its great affinity with DNA. Additionally, **Se-PC** exhibited strong superoxide radical ($O_2^{\bullet-}$) generation ability under light irradiation. Due to the interaction between DNA and **Se-PC**, the generated $O_2^{\bullet-}$ directly induced structural damage of DNA, ultimately leading to cell death. *In vitro* experiments showed that **Se-PC** effectively localized in the nucleus and achieved excellent killing performance against tumor cells. Benefiting from type-I characteristics, cell proliferation was also remarkably inhibited by the combination of **Se-PC** and excitation light even under severe hypoxic conditions (2% O_2). Furthermore, *in vivo* studies demonstrated that **Se-PC** exhibited notable efficacy in the photoablation of solid tumors, endowing **Se-PC** with great potential for advancing clinical translation of tumor PDT.

1 Introduction

Photodynamic therapy (PDT) has emerged as a promising clinical tumor treatment due to its non-invasive nature, localized action, repeatability and low toxicity.[1–3] Photosensitizers (PSs), the foundation of PDT, generate a large amount of highly toxic reactive oxygen species (ROS) upon light exposure to induce cell death. PSs can be categorized into two types: (1) type I, which produces superoxide anion radicals ($O_2^{\bullet-}$) or hydroxyl radicals (·OH) through electron transfer; (2) type II, which generates singlet oxygen ($^1O_2$) through energy transfer. Currently, most PSs predominantly rely on oxygen for type II PDT.[4,5] However, solid tumors often experience inadequate blood supply and high oxygen consumption, leading to insufficient oxygen delivery.[6,7] The low oxygen levels in solid tumors severely inhibit the efficiency of oxygen-dependent type II PDT, thereby diminishing its antitumor efficacy.[8] Notably, type I PDT exhibits reduced dependency on O_2 due to the oxygen cycle induced by the superoxide dismutase (SOD)-mediated dismutation reaction and Haber–Weiss/Fenton reaction, thereby exhibiting good performance in severe hypoxia of solid tumors.[9,10] However, the design of type I PSs is generally more challenging compared to type II PSs because the occurrence of the electron transfer process necessitates that PSs possess a suitable triplet energy level and maintain adequate close contact with the substrate and oxygen. To date, several type I organic PSs such as benzophenothiazine derivatives,[11–13] boron-dipyrromethene derivatives[14–16] and aggregation-induced emission luminogens[17–19] have been developed. Unfortunately, a clear understanding and rational design of type I PS systems still lag behind the increasing number of reports on type II PSs.

On the other hand, the therapeutic efficacy of PSs is inherently constrained by the limited diffusion distance (<0.02 μm) and short lifespan (<0.04 μs) of ROS, which restrict their ability to exert cytotoxic effects beyond their immediate microenvironment.[20–22] Consequently, the precise subcellular targeting of PSs emerges as a critical determinant of their therapeutic effectiveness, as it directly influences the spatial and temporal dynamics of ROS generation and their subsequent biological impact.[23,24] Organelles such as the plasma membrane, mitochondria, and nucleus are essential for maintaining cellular function.[25,26] Therefore, directing PSs to specific organelles can significantly enhance the efficiency of PDT.[27–29] Among them, the cell nucleus is considered an optimal target for antitumor therapy.[30,31] As the largest and most critical structure in eukaryotic cells, the nucleus has attracted

[a]*State Key Laboratory of Fine Chemicals, Frontiers Science Center for Smart Materials Oriented Chemical Engineering, Dalian University of Technology, Dalian 116024, China. E-mail: fanjl@dlut.edu.cn*

[b]*Liaoning Binhai Laboratory, Dalian, 116023, China*

[c]*Ningbo Institute of Dalian University of Technology, Ningbo 315016, China*

† Electronic supplementary information (ESI) available. See DOI: https://doi.org/10.1039/d5sc02476e

‡ Zipeng Li and Wenkai Liu contributed equally to this work.

widespread attention due to its essential role in cellular metabolism and genetic processes.[32] The genetic material (DNA and RNA) within the nucleus is actively involved in gene encoding, regulation and expression.[33,34] If ROS generated by PSs can directly oxidize nuclear DNA, thereby compromising genomic stability, they may circumvent the antioxidant protection mechanisms of tumor cells, resulting in a complete loss of cellular function.[35–37] However, PSs specifically designed to target nuclear DNA remain relatively scarce. This difficulty arises from the limited permeability of the nuclear pores to substances. Only small molecules, ions or certain specific proteins containing nuclear localization signals (NLS) can effectively traverse nuclear pores to enter the cell nucleus.[38] PSs often exhibit higher molecular weight, polarity, or charge, which hinders their ability to diffuse freely to the cell nucleus within the intracellular environment. Given the pivotal role of nuclear DNA in maintaining cellular integrity and its inherent susceptibility to oxidative damage, the development of type I PSs capable of selectively generating ROS within the nuclear compartment represents a compelling and urgent strategy to achieve targeted and effective tumor therapy.

Considering these critical factors, we integrated selenium atoms into the molecular framework of a pyridine cyanine dye, resulting in the design and synthesis of a novel nuclear DNA-targeted photosensitizer, **Se-PC**. **Se-PC** exhibits a high molar absorption coefficient and near-infrared absorption properties, making it particularly suitable for deep-tissue applications. The incorporation of selenium endows **Se-PC** with the ability to generate $O_2^{\bullet-}$ under low-dose irradiation (0.1 mW cm^{-2}) *via* a type I mechanism, as supported by theoretical calculations revealing a small S_1–T_1 energy gap and a large spin–orbit coupling (SOC) value, which promote an efficient intersystem crossing (ISC) process. Furthermore, **Se-PC** demonstrated a pronounced affinity for DNA and exceptional nuclear localization capabilities, as evidenced by fluorescence staining experiments. Agarose gel electrophoresis further confirmed that **Se-PC** induces significant gene damage through the degradation of nuclear DNA, ultimately triggering tumor cell death. Remarkably, **Se-PC**-mediated PDT achieves substantial reductions in cell viability under both normoxic and hypoxic conditions. *In vivo* studies using a tumor-bearing mouse model further underscore the exceptional therapeutic efficacy of **Se-PC** against solid tumors. Collectively, these findings position **Se-PC** as a highly promising nuclear DNA-targeting photosensitizer with significant potential for advancing tumor treatment strategies.

2 Results and discussion

2.1 Design and synthesis

In this study, we aimed to develop an efficient photosensitizer that targets cellular nuclear DNA for PDT. Asymmetric cyanine dyes have been extensively employed in the development of nucleic acid-binding probes. **S-PC** containing benzo[*d*]thiazole and *N*-aryl pyridine demonstrates exceptional targeting capability for cellular nuclear DNA, attracting significant attention.[39] Consequently, we substituted the sulfur atom in benzo[*d*]thiazole with a selenium atom to synthesize **Se-PC** (Fig. 1a). This incorporation of selenium will enhance the efficiency of intersystem crossing processes and promote the generation of ROS during PDT (Fig. 1b). The synthetic pathway for **Se-PC** is detailed in the ESI (Scheme S1).† First, 3-methoxybenzo[*d*]thiazole with iodoethane was reacted to yield the quaternized benzo[selen]thiazole derivative. Subsequently, thermal condensation with *N*,*N*-diphenylformamidine was performed to produce the intermediate of the asymmetric cyanine dye. Finally, the target compound **Se-PC** was synthesized through a condensation reaction catalyzed by acetic anhydride and *N*,*N*-diisopropylethylamine, which involved the asymmetric cyanine dye intermediate and *N*-aryl pyridine salt. The molecular structure was characterized using NMR spectroscopy and high-resolution mass spectrometry (HR-MS) with specific details provided in Fig. S15–S21.†

2.2 Photophysical properties of Se-PC with DNA

The interaction between **Se-PC** and DNA was initially investigated using calf thymus DNA (CT DNA), which serves as a representative model for double-stranded DNA (dsDNA). Ultraviolet-visible (UV-vis) absorbance spectroscopy demonstrated that **Se-PC** displayed a strong absorption peak within the range of 500–625 nm. Notably, a new absorption peak in the range of 550–650 nm was observed in the presence of CT DNA (Fig. 1c) with the maximum absorption wavelength shifting to 620 nm. Meanwhile, the isolated **Se-PC** exhibited weak fluorescence. By contrast, in the presence of CT DNA, the fluorescence intensity of **Se-PC** at its maximum emission wavelength (650 nm) increased by 69-fold (Fig. 1d). To elucidate whether the fluorescence activation mechanism of **Se-PC** depends on specific DNA binding, *in vitro* digestion experiments with DNase and RNase were conducted. The results demonstrated that treatment with DNase led to a significant decrease in the fluorescence intensity of **Se-PC** at 650 nm, whereas no obvious fluorescence change was observed in the RNase A-treated group (Fig. S1†). These findings confirm that the fluorescence activation of **Se-PC** was indeed DNA-dependent. Besides, the fluorescence responses of **Se-PC** to various oligonucleotides (Table S2†),[40,41] including the double stranded DNA structure (pure AT sequence, pure GC sequence, and mixed sequence), single stranded DNA structure (ssDNAmix), G-quadruplex structure (c-MYC, Tel26, hTelo_G4), circular mitochondrial DNA (Mito 0.5–22, Mito 0.5–22 cs, and Mito), and single stranded RNA structure (NC, ssRNAmix), were assessed. As shown in Fig. 1e, the fluorescence signals of **Se-PC** only exhibited a slight increase upon addition of non-dsDNA including single-stranded DNA, G4 DNA, mitochondrial DNA, and RNA. Conversely, dramatic fluorescence enhancements were observed upon addition of $ds(AT)_{20}$ or $dsDNA_{mix}$. These results suggested that **Se-PC** specifically interacted with dsDNA, particularly with double stranded nucleic acid sequences that are rich in AT base pairs.

To elucidate the interaction mechanism between **Se-PC** and DNA, three distinct double-stranded DNA models (PDB: 7YZ7, 111D, and 2GYX) were selected for molecular docking calculations. As demonstrated in Fig. 1f and S2,† **Se-PC** bound within the minor groove of dsDNA *via* hydrophobic interactions and

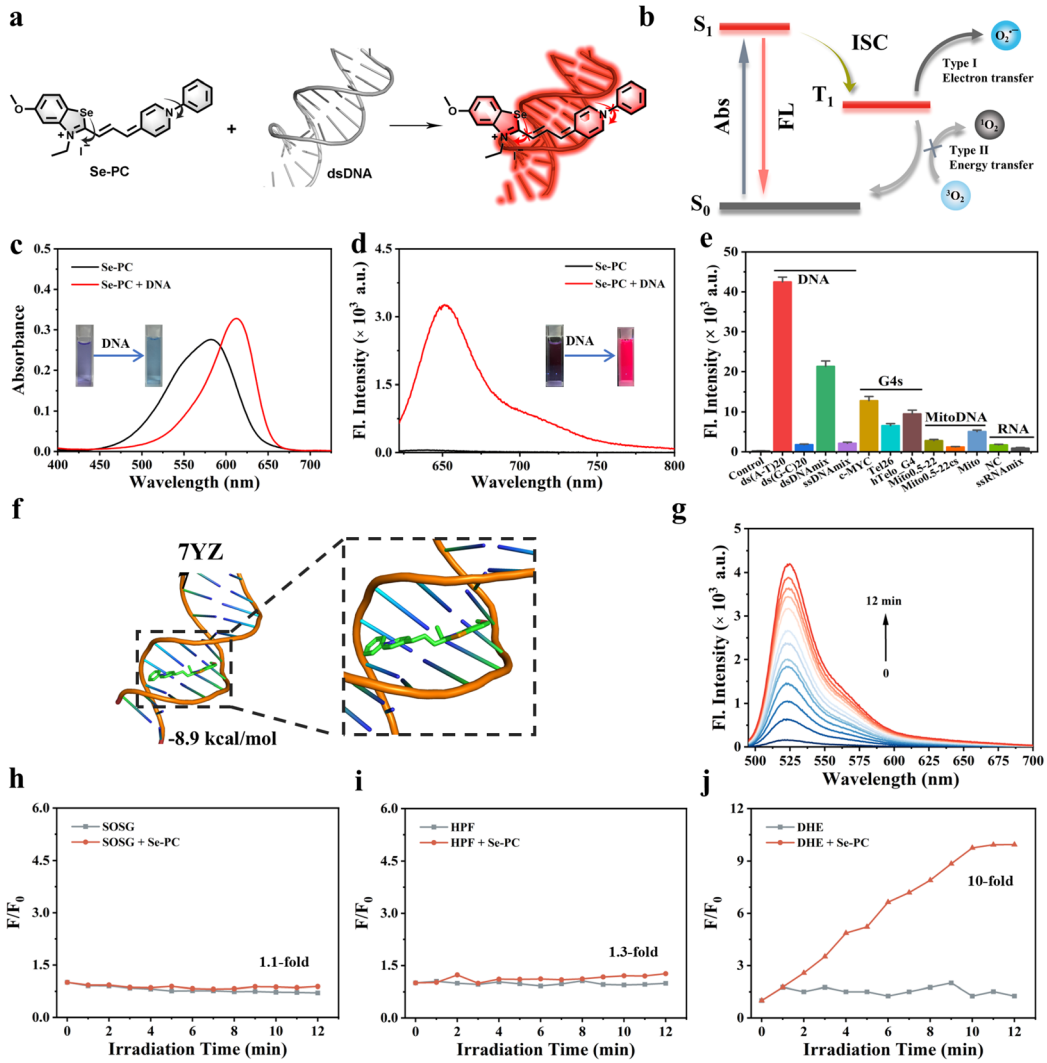

Fig. 1 (a) Schematic illustration of **Se-PC** binding to dsDNA. (b) The proposed mechanism for efficient photodynamic therapy. (c) UV-vis absorption spectra and (d) fluorescence spectra of **Se-PC** (4 μM) in the absence or presence of CT DNA (100 μg mL^{-1}) in 10 mM PBS buffer (300 mM NaCl, pH 7.4). (e) Fluorescence intensity of **Se-PC** (1.0 μM) at 650 nm in response to various oligonucleotides (4.0 μM). (f) Molecular docking calculation of **Se-PC** with dsDNA (7YZ7, 111D, and 2GYX). (g) Fluorescence spectra of DCFH (10 μM) for **Se-PC** after irradiation (0.1 mW cm^{-2}) for different time periods. (h) Fluorescence intensities of SOSG (0.5 μM) at 525 nm, (i) fluorescence intensities of HPF (10 μg mL^{-1}) at 515 nm and (j) fluorescence intensities of DHE (10 μM) at 610 nm with irradiation (0.1 mW cm^{-2}) or without irradiation for different time periods.

van der Waals forces. This binding restricted the torsion of **Se-PC** conformation and rotation of single bonds, consequently enhancing fluorescence. The binding energies of **Se-PC** with DNA models (PDB: 7YZ7, 111D, and 2GYX) were 8.9 kcal mol^{-1}, 8.4 kcal mol^{-1}, and 8.2 kcal mol^{-1}, respectively. These findings indicated that the affinity of **Se-PC** with DNA was significantly strong, supporting the conclusions drawn from solution tests. The above experimental results demonstrated that despite selenium atom substitution and *N*-arylpyridine structural modification, **Se-PC**, as a derivative of SYBR dye,[42] retains the core characteristic of its parent compound: specific recognition and binding to the DNA minor groove (particularly AT-rich sequences), resulting in fluorescence enhancement. This indicated that the key structural modifications did not alter its fundamental DNA interaction mode.

2.3 ROS detection

Then the efficiency of total ROS generation was evaluated by a general indicator (2,7-dichlorodihydrofluorescein, DCFH), whose fluorescence at 525 nm can be produced by any type of ROS. As depicted in Fig. S3† and 1g, **Se-PC** displayed significant ROS generation efficiency. To elucidate the types of ROS generated, the specific probes were utilized: singlet oxygen sensor green (SOSG) for the detection of $^1O_2$, dihydroethidium (DHE) for the detection of $O_2^{\cdot-}$, and hydroxyphenyl fluorescein (HPF) for detecting hydroxyl radicals (·OH). As illustrated in Fig. 1h and i, SOSG showed 1.1-fold SOSG fluorescence enhancement in the presence of **Se-PC**. Similarly, 1.3-fold HPF fluorescence enhancement was observed under comparable conditions, indicating a minor production of $^1O_2$ and ·OH. In contrast, Fig. 1j demonstrated that the presence of **Se-PC** under

light irradiation resulted in 10-fold DHE fluorescence enhancement.

To elucidate whether the DHE fluorescence enhancement originates from specific oxidation by $O_2^{\bullet-}$, the fluorescence emission spectra of different mixtures under 488 nm excitation were analyzed (Fig. S4†). The **Se-PC** + DNA mixture exhibited stable fluorescence at 650 nm, representing the intrinsic signal of the **Se-PC**-DNA complex; The DHE + **Se-PC** group showed limited fluorescence enhancement, indicating weak fluorescence signals from the oxidation product 2-hydroxyethidium in the absence of DNA. In the DHE + **Se-PC** + DNA system, dual emission peaks at 600 nm and 650 nm displayed a synergistic increasing trend with prolonged illumination time. These results conclusively demonstrated that the fluorescence enhancement at 600 nm specifically reflects the oxidation process of DHE by $O_2^{\bullet-}$, rather than being caused by **Se-PC**–DNA interactions. Additionally, the mass spectrometry data (Fig. S5†) clearly identified the formation of 2-hydroxyethidium (2-OH-E^+), as evidenced by the characteristic *m*/*z* peak at 330.1 [M^+]. In addition, to confirm the above experimental results, electron paramagnetic resonance (EPR) measurements were conducted. Under dark and light irradiation conditions, no signal was generated in the EPR spectra of 2,2,6,6-tetramethyl-4-piperidone (TEMP) with **Se-PC**, indicating that **Se-PC** does not have the ability to produce $^1O_2$ (Fig. S6†). In contrast, typical EPR signals of $O_2^{\bullet-}$ were captured from the irradiated solutions of DMPO with **Se-PC**, consistent with fluorescence probe data. Collectively, these results suggested that **Se-PC** mainly generated $O_2^{\bullet-}$ *via* type I mechanisms.

To investigate the detailed mechanism of triplet state formation, theoretical calculations on the optimized structures of **S-PC** and **Se-PC** were performed using time-dependent density functional theory (TD-DFT). As illustrated in Fig. S7 and Table S1,† the ΔE_{S1-T1} values of **S-PC** and **Se-PC** were 0.70 eV and 0.64 eV, respectively, indicating that the incorporation of selenium decreases ΔE_{S1-T1}. Furthermore, the SOC value of **Se-PC** (0.55 cm^{-1}) was an order of magnitude greater than that of **S-PC** (0.046 cm^{-1}). Consequently, the lower ΔE_{S1-T1} energy gap and higher SOC value indicated that **Se-PC** exhibited enhanced propensity for ISC under light irradiation. Moreover, the ΔE_{T1-S0} energy gap of **Se-PC** was determined to be 1.35 eV (Fig. S8 and Table S1†), lower than the 1.61 eV threshold required for exciting O_2 to generate $^1O_2$ through energy transfer.[20,43] Therefore, **Se-PC** tends to return to the ground state *via* electron transfer following irradiation, generating $O_2^{\bullet-}$.

2.4 Nuclear targeting ability of Se-PC

The cellular uptake and subcellular distribution of **Se-PC** are critical determinants of its therapeutic efficacy. Initially, uptake experiments were conducted using MCF-7, 4T1, HeLa, and L929 cells. The results (Fig. 2a and S9†) revealed that **Se-PC** could rapidly accumulate into the cell nuclei just within 1.5 h.

Considering that DNA is primarily distributed in the mitochondria and the cell nucleus, the co-staining experiments of **Se-PC** with mitochondrial tracker MitoTracker green (**MTG**) were conducted. As shown in Fig. 2b, the boundary between the green fluorescence signal of **MTG** and the red fluorescence

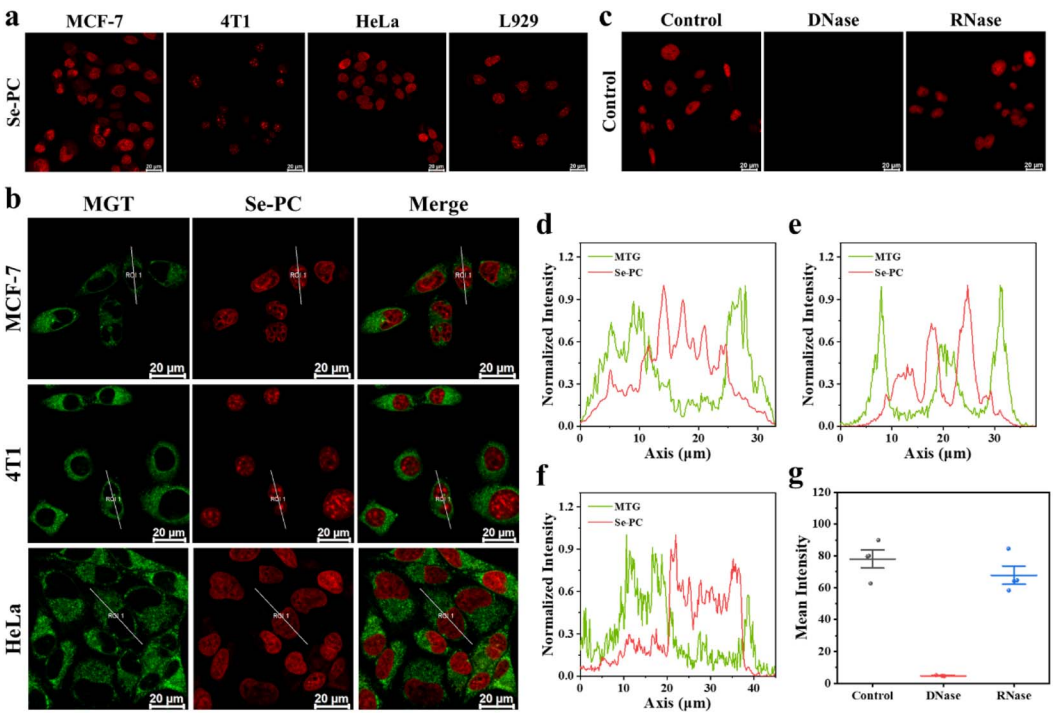

Fig. 2 (a) Confocal images of MCF-7, 4T1, HeLa and L929 cells co-stained with **Se-PC** (1 μM), respectively. (b) Confocal images of MCF-7, 4T1 and HeLa cells co-stained with **Se-PC** (1 μM) and **MTG** (1 μM), respectively. (c) Confocal images of fixed MCF-7 cells co-stained with **Se-PC** (1 μM) following treatment with DNase I (100 U mL^{-1}) or RNase A (100 μg mL^{-1}), respectively. (d–f) Curve chart: intensity correlation of **Se-PC** and **MTG** in (b). (d) ROI of MCF-7 cells, (e) ROI of 4T1 cells and (f) ROI of HeLa cells. (g) Mean fluorescence intensity of **Se-PC** in (c). Scale bar: 20 μm.

signal of **Se-PC** was distinctly evident. Additionally, the intensity spectrum of the green line in the region of interest (ROI) revealed asynchronous fluorescence signals of **MTG** and **Se-PC** (Fig. 2d–f). Moreover, digestion experiments with deoxyribonuclease (DNase) and ribonuclease (RNase) were conducted (Fig. 2c and g). Following DNase digestion of nuclear DNA, the red fluorescence of **Se-PC** diminishes, suggesting a robust interaction between **Se-PC** and DNA. Conversely, red fluorescence was observed after RNase-mediated RNA digestion. These findings implied that the pronounced nuclear targeting capacity of **Se-PC** was closely linked to its interaction with nuclear DNA.

2.5 ROS generation ability of Se-PC within cells

The total ROS generated in MCF-7 cells during the PDT process was calculated using 2′,7′-dichlorodihydrofluorescein diacetate

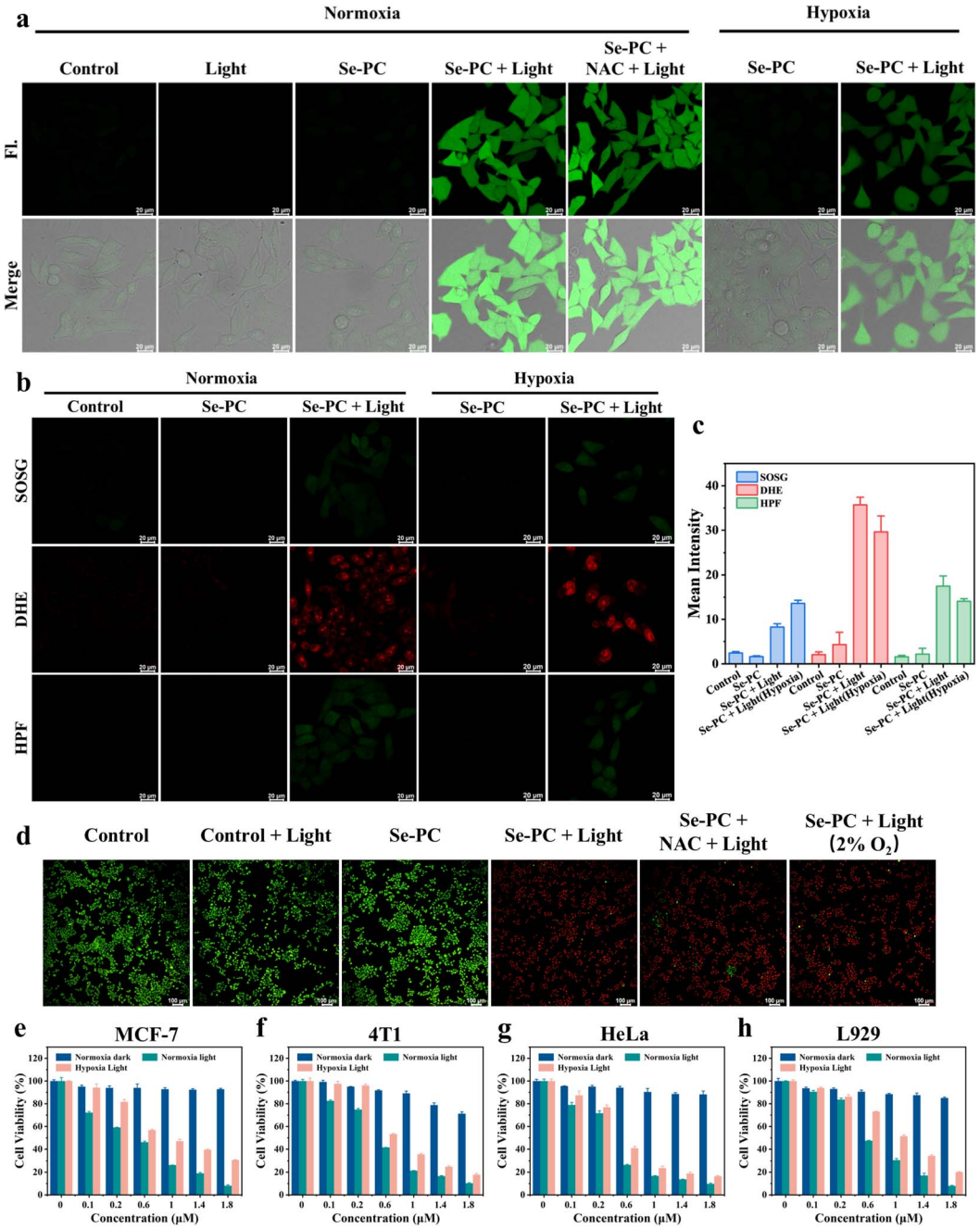

Fig. 3 Intracellular ROS production induced by **Se-PC** (1 μM) in MCF-7 cells under different conditions, monitored using specific ROS indicators. (a) The total ROS indicator DCFH-DA. (b) The $^1O_2$ indicator SOSG, the $O_2^{\bullet-}$ indicator DHE and the ·OH indicator HPF. (c) Quantitative analysis corresponding to (a) and (b). Scale bar: 20 μm. (d) Confocal images of MCF-7 cells co-stained with the calcium-AM/PI test kit after different treatments. Scale bar: 100 μm. Cell viability of (e) MCF-7, (f) 4T1, (g) HeLa and (h) L929 cells co-incubated with different concentrations of **Se-PC** after different treatments.

(DCFH-DA, ROS indicator). As illustrated in Fig. 3a, the ROS amounts of **Se-PC**-treated cells under both normoxic (21% O_2) and hypoxic (2% O_2) conditions were significantly higher than those in the control group, even when pretreated with *N*-acetylcysteine (NAC, antioxidant).[44,45] This observation suggested that ROS accumulation predominantly occurs in the cell nucleus upon illumination and is unaffected by intracellular reducing agents. To further elucidate the types of ROS generated in the cellular microenvironment (Fig. 3b and c), SOSG was first utilized to detect the production of $^1O_2$ within the MCF-7 cells. Experimental data indicated the presence of a small amount of $^1O_2$ under both normoxic and hypoxic conditions. To further validate the light-dose dependency of $^1O_2$ generation, additional solution-phase analyses were performed under matched irradiation conditions (5 mW cm^{-2}, 5 min) to the cellular studies. As shown in Fig. S10a,† the SOSG fluorescence intensity (F/F_0) only increased by 1.41 times even at this higher light dose. Complementary EPR measurements (Fig. S10b†) did not detect the $^1O_2$ signal, confirming that $^1O_2$ production in solution was negligible regardless of light intensity. When DHE was used to assess intracellular $O_2^{\bullet-}$, the findings corroborated those observed in the total ROS test. DHE exhibited a significant increase in red fluorescent signal after light irradiation, thereby confirming the generation of type I ROS in cells. Furthermore, ·OH detection with HPF revealed higher ·OH production compared to the *in vitro* system. This was because intracellular superoxide dismutase (SOD) converted $O_2^{\bullet-}$ to H_2O_2, which then generated ·OH *via* the Fenton reaction—a behavior consistent with other type I photosensitizers.[27] These results collectively indicated that **Se-PC** possessed mainly type I photodynamic activity in living cells.

2.6 The phototherapeutic effect of Se-PC in cells

The robust generation of $O_2^{\bullet-}$ prompted us to assess the cytotoxic effects of **Se-PC** using a live/dead cell co-staining assay (Fig. 3d). In this assay, living cells were stained with calcein AM, emitting green fluorescence, while dead cells were stained with propidium iodide (PI), emitting red fluorescence. Notably, cells treated with **Se-PC** followed by irradiation (**Se-PC** + light) exhibited pronounced cell death under both normoxic and hypoxic conditions. In addition, the standard MTT assay (Fig. 3e) revealed that **Se-PC** exhibited low cytotoxicity under dark conditions (IC_{50} = 16.57 μM, Table S3†). After light exposure (5 mW cm^{-2}, 5 min) under normoxic conditions, **Se-PC** effectively induced tumor cell death (IC_{50} = 0.33 μM). Equally, substantial phototoxicity of **Se-PC** toward MCF-7 cells was still obtained under hypoxic conditions (IC_{50} = 0.86 μM). Notably, we pre-treated the cells with 1 mM NAC for 4 hours to sustain a high concentration of reducing agents within the cells (Fig. S11†). Even following light exposure, **Se-PC** continued to effectively induce tumor cell death (IC_{50} = 0.59 μM). These findings suggested that **Se-PC** conferred significant advantages in the elimination of tumor cells.

To further elucidate the photosensitizing efficacy and broad-spectrum anti-proliferative activity of **Se-PC**, we assessed its cytotoxicity against several other cells (4T1, HeLa and L929). As demonstrated in Fig. 3f–h, the cells were treated with varying concentrations of **Se-PC** and subsequently exposed to light irradiation under normoxic or hypoxic conditions. The results indicated that dose-dependent cell death was observed across all three cell lines. In the normoxic group, the IC_{50} values for 4T1, HeLa, and L929 cells were 0.38 μM, 0.29 μM, and 0.49 μM,

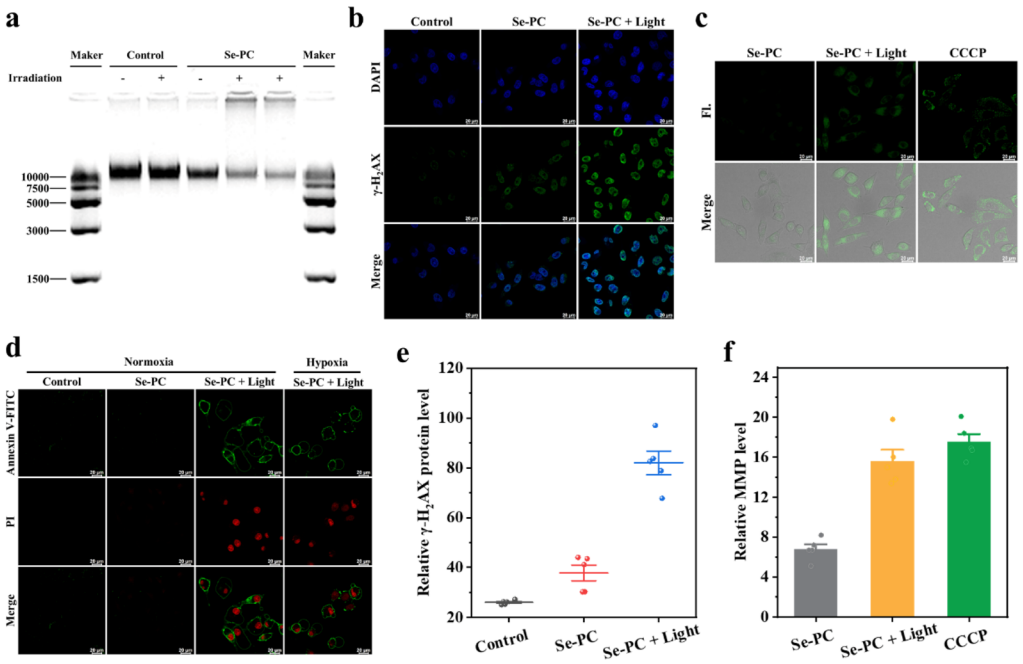

Fig. 4 (a) Agarose gel electrophoresis of MCF-7 cells subjected to different treatments. (b) Analysis of γ-H_2AX protein expression in MCF-7 cells subjected to different treatments. (c) Analysis of mitochondrial membrane potential in MCF-7 cells subjected to different treatments, CCCP served as a positive control. (d) Analysis of apoptosis in MCF-7 cells subjected to different treatments. (e and f) Quantitative analysis of γ-H_2AX protein corresponding to (b) and MMP corresponding to (c), respectively. Data were expressed as the mean ± SD (n = 5).

respectively (Table S3†). In the hypoxic group, the IC_{50} values remained consistent (0.67 μM, 0.43 μM, and 0.94 μM). These results suggested that **Se-PC** displayed significant phototoxicity in both normoxic and hypoxic environments, attributable to its type I photodynamic properties, which effectively overcome the limitations of traditional oxygen-dependent PDT.

2.7 The apoptosis mechanism induced by Se-PC

To further investigate the mechanism of cell death, intracellular DNA content was first evaluated using agarose gel electrophoresis. As shown in Fig. 4a, a distinct band was observed in the control group. Remarkably, **Se-PC** photooxidized the nucleic acid bands in a dose-dependent manner under illumination. Since phosphorylated H_2AX at serine 139 (γ-H_2AX) serves as a specific indicator of DNA damage, immunofluorescence staining was utilized to confirm the occurrence of genetic damage. As illustrated in Fig. 4b and e, no DNA damage signals were observed in the control group. In contrast, the cells displayed increased green fluorescence of γ-H_2AX in the nucleus after treatment with light irradiation, indicating that PDT resulted in DNA damage. Besides, the mitochondrial membrane potential (MMP) detection assay revealed that **Se-PC** induced remarkable reduction in MMP compared to the control group (Fig. 4c and f). To further examine cell apoptosis, Annexin V-FITC and PI staining were performed. As shown in Fig. 4d and S12,† the simultaneous presence of Annexin V (+) and PI (+) fluorescence signals and flow cytometry assay data in the **Se-PC** + light group indicated that these cells underwent late apoptotic processes without oxygen dependence (normoxia: 88.2%, hypoxia: 83.4%). The findings collectively indicated that **Se-PC** efficiently localized within nuclear DNA, where light irradiation triggered the generation of ROS, causing substantial oxidative damage to the genetic material and ultimately activating the apoptotic pathway.[46,47]

2.8 The anti-tumor effect of Se-PC *in vivo*

Based on the significant *in vitro* results, the feasibility of **Se-PC** *in vivo* tumor treatment was investigated. The tumor-bearing mouse model was established using 4T1 cells. The intratumoral injection assay (Fig. 5b and c) *in vivo* first revealed that **Se-PC** can rapidly penetrate into the tumor and remain stable for 3 h. Then, the tumor therapeutic effect of **Se-PC** was

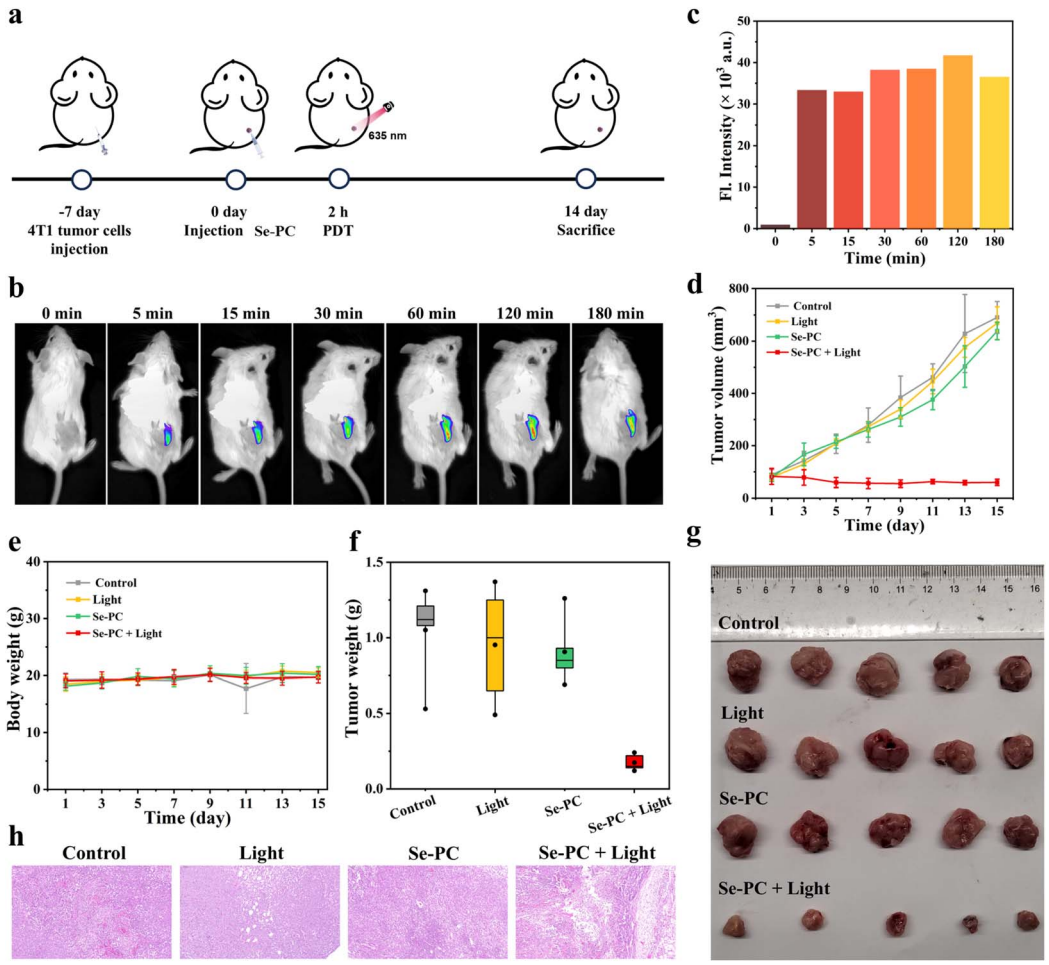

Fig. 5 (a) Workflow for the treatment of **Se-PC**. (b) *In vivo* fluorescence imaging of 4T1-bearing mice post-injecting **Se-PC**. (c) The quantitative fluorescence intensity of **Se-PC**. (d) Relative tumor volume of 4T1-bearing mice after various treatments. (e) Change of tumor weights and (f) mice weights after various treatments. (g) Photographs of excised tumors and (h) H&E staining of primary tumors in different treatment groups. Data were expressed as the mean ± SD ($n = 5$).

evaluated. The mice were categorized into four groups: control, control + light, **Se-PC**, and **Se-PC** + light. All mice received injection of PBS or **Se-PC**. The tumor sites of the control + light and **Se-PC** + light groups were illuminated with 635 nm LED light (50 mW cm^{-2}, 10 min) two hours post-injection. Then, the tumor size was measured using a Vernier caliper every two days from day 0 to day 14 following treatment. As illustrated in Fig. 5d, only the **Se-PC** + light group demonstrated a significant tumor-suppressing phenomenon. After 14 days, the tumor volume in the **Se-PC** + light group decreased to 8.6%. Additionally, no noticeable abnormal body weight changes were observed in mice across all groups during this process (Fig. 5e). To further assess the anti-tumor effects of **Se-PC**, all mice were euthanized at the conclusion of the 14-day treatment period, and the tumors were excised for further examination. The excised tumors were weighed and photographed. As shown in Fig. 5f and g, the tumor weight in the **Se-PC** + light group was significantly lower than that in the control group, with a maximum inhibition rate of up to 83.4% compared to the control group. Hematoxylin and eosin (H&E) histological analysis (Fig. 5h) revealed that tumor sections from the **Se-PC** + light group exhibited compromised tissue structure and nuclear shrinkage. Immunofluorescence staining revealed a significant decrease in Ki67 expression levels (reduced red fluorescence intensity) in tumor tissues of the treatment group compared to the control group (Fig. S13†). This finding was consistent with the observed tumor growth inhibition, demonstrating that **Se-PC** possesses remarkable anti-proliferative effects. In addition, the histological analysis confirmed that no significant pathological changes were observed in the organs of heart, liver, spleen, lung, and kidney from mice across the different treatment groups (Fig. S14†), supporting the biosafety profile of the therapeutic approach. Overall, the *in vivo* results suggested that **Se-PC** displayed significant anti-tumor efficacy.

3 Conclusions

In conclusion, we have developed a novel photosensitizer, **Se-PC**, designed to directly target nuclear DNA for effective PDT in tumor treatment. Our studies demonstrated that **Se-PC** exhibited strong DNA-binding affinity and enhanced fluorescence properties *in vitro*, along with the ability to generate $O_2^{\bullet-}$ under low-dose irradiation (0.1 mW cm^{-2}). Theoretical calculations revealed that **Se-PC** possessed a small S_1–T_1 energy gap (0.64 eV) and a high SOC value (0.55 cm^{-1}), which facilitate an efficient ISC process, underpinning its unique type I PDT mechanism. Additionally, **Se-PC** effectively localized in the cell nucleus and produced $O_2^{\bullet-}$ under both normoxic and hypoxic conditions, inducing DNA damage and ultimately triggering apoptosis in tumor cells. Remarkably, **Se-PC** exhibited potent cytotoxicity, as evidenced by nanomolar IC_{50} values across four distinct cell lines. Moreover, in a tumor-bearing mouse model, the combination of **Se-PC** and light irradiation significantly suppressed tumor growth, highlighting its considerable potential for clinical translation. Collectively, these findings underscore **Se-PC** as a highly promising therapeutic reagent for clinical tumor treatment.

Data availability

The data supporting this article have been included as part of the ESI.†

Author contributions

Z. P. Li was responsible for the initial study design and manuscript writing. Z. P. Li and W. K. Liu formed most of the experiments. W. Y. Ma and C. Y. Zhang were responsible for conducting the safety assessment assays. J. L. Fan contributed to analysis of the data and manuscript revision. X. J. Peng supervised the work.

Conflicts of interest

The authors declare that they have no known competing financial interests or personal relationships that could have appeared to influence the work reported in this paper.

Acknowledgements

This work was financially supported by the National Natural Science Foundation of China (22338005 and 22494701), Science and Technology Innovation Yongjiang 2035 (2024Z218 and 2024Z185), Liaoning Binhai Laboratory (LBLB-2023-03), Liaoning Provincial Science and Technology Joint Fund (2023JH2/101800039 and 2023JH2/101800037) and the Fundamental Research Funds for the Central Universities (DUT22LAB601). The animal protocol was approved by the local research ethics review board of the Animal Ethic Committee of Dalian University of Technology (DUT20230322).

Notes and references

1 G. Obaid, J. P. Celli, M. Broekgaarden, A.-L. Bulin, P. Uusimaa, B. Pogue, T. Hasan and H.-C. Huang, *Nat. Rev. Bioeng.*, 2024, **2**, 752–769.
2 E. Nestoros, A. Sharma, E. Kim, J. S. Kim and M. Vendrell, *Nat. Rev. Chem.*, 2025, **9**, 46–60.
3 X. Yuan, J.-L. Zhou, L. Yuan, J. Fan, J. Yoon, X.-B. Zhang, X. Peng and W. Tan, *Sci. China: Chem.*, 2024, **68**, 826–865.
4 V.-N. Nguyen, Y. Yan, J. Zhao and J. Yoon, *Acc. Chem. Res.*, 2021, **54**, 207–220.
5 H. Kim, Y. R. Lee, H. Jeong, J. Lee, X. Wu, H. Li and J. Yoon, *Smart Mol.*, 2023, **1**, e20220010.
6 Z. Chen, F. Han, Y. Du, H. Shi and W. Zhou, *Signal Transduction Targeted Ther.*, 2023, **8**, 70–93.
7 E. N. Arner and J. C. Rathmell, *Cancer Cell*, 2023, **41**, 421–433.
8 M. Li, Y. Shao, J. H. Kim, Z. Pu, X. Zhao, H. Huang, T. Xiong, Y. Kang, G. Li, K. Shao, J. Fan, J. W. Foley, J. S. Kim and X. Peng, *J. Am. Chem. Soc.*, 2020, **142**, 5380–5388.
9 B. Lu, L. Wang, H. Tang and D. Cao, *J. Mater. Chem. B*, 2023, **11**, 4600–4618.
10 J. Sun, K. Du, J. Diao, X. Cai, F. Feng and S. Wang, *Angew. Chem., Int. Ed.*, 2020, **59**, 12122–12128.

11 T. Xiong, Y. Chen, Q. Peng, S. Lu, S. Long, M. Li, H. Wang, S. Lu, X. Chen, J. Fan, L. Wang and X. Peng, *Adv. Mater.*, 2024, **36**, 2309711–2309721.
12 Z. Wang, W. Ma, Z. Yang, D. O. Kiesewetter, Y. Wu, L. Lang, G. Zhang, S. Nakuchima, J. Chen, Y. Su, S. Han, L.-G. Wu, A. J. Jin and W. Huang, *J. Am. Chem. Soc.*, 2024, **146**, 28973–28984.
13 M. Li, T. Xiong, J. Du, R. Tian, M. Xiao, L. Guo, S. Long, J. Fan, W. Sun, K. Shao, X. Song, J. W. Foley and X. Peng, *J. Am. Chem. Soc.*, 2019, **141**, 2695–2702.
14 Y. Zhu, F. Wu, B. Zheng, Y. Yang, J. Yang and H. Xiong, *Nano Lett.*, 2024, **24**, 8287–8295.
15 Z. Fan, K.-X. Teng, Y.-Y. Xu, L.-Y. Niu and Q.-Z. Yang, *Angew. Chem., Int. Ed.*, 2025, **64**, e202413595.
16 K. X. Teng, W. K. Chen, L. Y. Niu, W. H. Fang, G. Cui and Q. Z. Yang, *Angew. Chem., Int. Ed.*, 2021, **60**, 19912–19920.
17 J. Liu, X. Ou, K. Wang, K. Wang, L. Gui, F. Song, C. Chen, J. W. Y. Lam, Z. Yuan and B. Z. Tang, *Adv. Funct. Mater.*, 2024, **34**, 2410202–2410212.
18 L. Liu, C. Li, J. Gong, Y. Zhang, W. Ji, L. Feng, G. Jiang, J. Wang and B. Z. Tang, *Angew. Chem., Int. Ed.*, 2023, **62**, e202307776.
19 J. Zhuang, B. Wang, H. Chen, K. Zhang, N. Li, N. Zhao and B. Z. Tang, *ACS Nano*, 2023, **17**, 9110–9125.
20 C. Xiang, Y. Liu, Q. Ding, T. Jiang, C. Li, J. Xiang, X. Yang, T. Yang, Y. Wang, Y. Tan, L. Mei, Z. Lu, J. S. Kim and P. Gong, *Adv. Funct. Mater.*, 2024, 2417979–2417990, DOI: **10.1002/adfm.202417979**.
21 M. Ochsner, *J. Photochem. Photobiol., B*, 1997, **39**, 1–18.
22 M. Niedre, M. S. Patterson and B. C. Wilson, *Photochem. Photobiol.*, 2002, **75**, 382–391.
23 Y. Li, Y. Song, J. Yin, W. Pan, N. Li and B. Tang, *Chem. Commun.*, 2024, **60**, 8170–8185.
24 P. Gao, W. Pan, N. Li and B. Tang, *ACS Appl. Mater. Interfaces*, 2019, **11**, 26529–26558.
25 R. Wang, X. Li and J. Yoon, *ACS Appl. Mater. Interfaces*, 2021, **13**, 19543–19571.
26 K.-M. Liu, Y. Wang, F.-W. Xia, S. Feng, X.-Q. Yu and M.-Y. Wu, *Smart Mol.*, 2025, e20240060.
27 W. Chen, Y. Zhang, H. B. Yi, F. Wang, X. Chu and J. H. Jiang, *Angew. Chem., Int. Ed.*, 2023, **62**, e202300162.
28 S. Zeng, Y. Wang, C. Chen, H. Kim, X. Liu, M. Jiang, Y. Yu, Y. S. Kafuti, Q. Chen, J. Wang, X. Peng, H. Li and J. Yoon, *Angew. Chem., Int. Ed.*, 2024, **63**, e202316487.
29 Y. Jiang, S. Huang, H. Ma, J. Weng, X. Du, Z. Lin, J. Kim, W. You, H. Zhang, D. Wang, J. S. Kim and H. Sun, *J. Am. Chem. Soc.*, 2024, **146**, 25270–25281.
30 L. Pan, J. Liu and J. Shi, *Chem. Soc. Rev.*, 2018, **47**, 6930–6946.
31 Y. Chen, J. Xu, X. Liu, L. Guo, P. Yi and C. Cheng, *MedComm*, 2023, **4**, e421.
32 K. F. Blount and O. C. Uhlenbeck, *Annu. Rev. Biophys.*, 2005, **34**, 415–440.
33 J. L. Childs Disney, X. Yang, Q. M. R. Gibaut, Y. Tong, R. T. Batey and M. D. Disney, *Nat. Rev. Drug Discovery*, 2022, **21**, 736–762.
34 J. Sheng, J. Gan and Z. Huang, *Med. Res. Rev.*, 2013, **33**, 1119–1173.
35 M. Kang, Z. Zhang, W. Xu, H. Wen, W. Zhu, Q. Wu, H. Wu, J. Gong, Z. Wang, D. Wang and B. Z. Tang, *Adv. Sci.*, 2021, **8**, 2100524–2100537.
36 K.-N. Wang, L.-Y. Liu, D. Mao, M.-X. Hou, C.-P. Tan, Z.-W. Mao and B. Liu, *Angew. Chem., Int. Ed.*, 2022, **61**, e202114600.
37 P. Li, Y. Du, J. Qiu, D. Li, G. Li and G. Shan, *Adv. Healthcare Mater.*, 2023, **12**, 2301517–2301527.
38 Y. Sakiyama, A. Mazur, L. E. Kapinos and R. Y. H. Lim, *Nat. Nanotechnol.*, 2016, **11**, 719–723.
39 Z. Li, Z. Liu, D. Yu, Q. Yao, W. Ma, C. Zhang, J. Fan and X. Peng, *Chem. Sci.*, 2024, **15**, 17524–17532.
40 A. Pandith, Y. Luo, Y. Jang, J. Bae and Y. Kim, *Angew. Chem., Int. Ed.*, 2023, **62**, e202215049.
41 H. Sun, R. Sun, D. Yang, Q. Li, W. Jiang, T. Zhou, R. Bai, F. Zhong, B. Zhang, J. Xiang, J. Liu, Y. Tang and L. Yao, *J. Am. Chem. Soc.*, 2024, **146**, 22736–22746.
42 J. M. Alaranta, K.-N. Truong, M. F. Matus, S. A. Malola, K. T. Rissanen, S. S. Shroff, V. S. Marjomäki, H. J. Häkkinen and T. M. Lahtinen, *Dyes Pigments*, 2022, **208**, 110844.
43 M. Y. Wu, Z. J. Wu, J. L. Wang, C. Kam, T. Y. Chou, S. Feng, K. Li and S. Chen, *ACS Mater. Lett.*, 2024, **6**, 4533–4544.
44 W. Muhammad, M. Liang, B. Wang, J. Xie, W. Ahmed and C. Gao, *Biomacromolecules*, 2025, **26**, 528–540.
45 D. Ezeriņa, Y. Takano, K. Hanaoka, Y. Urano and T. P. Dick, *Cell Chem. Biol.*, 2018, **25**, 447–459.
46 S. Rangasamy, H. Ju, S. Um, D.-C. Oh and J. M. Song, *J. Med. Chem.*, 2015, **58**, 6864–6874.
47 M. Redza-Dutordoir and D. A. Averill-Bates, *Biochim. Biophys. Acta, Mol. Cell Res.*, 2016, **1863**, 2977–2992.